Journal of Power Sources 269 (2014) 694–703

Contents lists available at ScienceDirect

Journal of Power Sources

journal homepage: www.elsevier.com/locate/jpowsour

A study of 40 Ah lithium ion batteries at zero percent state of charge as a function of temperature

Pierrot S. Attidekou [a, *], Simon Lambert [b], Matthew Armstrong [b], James Widmer [b], Keith Scott [c], Paul A. Christensen [a]

[a] School of Chemical Engineering and Advanced Materials, Newcastle University, Bedson Building, Newcastle upon Tyne NE1 7RU, UK
[b] School of Electrical and Electronic Engineering, Newcastle University, Merz Court, Newcastle upon Tyne NE1 7RU, UK
[c] School of Chemical Engineering and Advanced Materials, Newcastle University, Merz Court, Claremont Road, Newcastle upon Tyne NE1 7RU, UK

HIGHLIGHTS

- 40 Ah, Saft batteries were studied using EIS at 0% SOC as function of temperature.
- The batteries were modelled using the equivalent circuit approach.
- EIS spectra exhibit superimposed impedance arcs that are temperature dependent.
- Non-viable and viable batteries could be discriminated.
- Activation energy, polarisation resistance and time constant could be extracted.

ARTICLE INFO

Article history:
Received 29 November 2013
Received in revised form
9 June 2014
Accepted 11 June 2014
Available online 18 June 2014

Keywords:
High power lithium ion batteries
State of charge
Electrochemical Impedance Spectroscopy (EIS)
Constant phase element (CPE)
Solid Electrolyte Interface (SEI)
Activation energy

ABSTRACT

A theoretical equivalent circuit model of two 40 Ah commercial batteries supplied by Saft was formulated to interpret electrochemical impedance spectra as a function of temperature at zero state-of-charge. The batteries were chosen to represent viable and non-viable products from the Saft production line. This paper is the first contribution from a project in Newcastle to develop a rapid, non-destructive analytical method for quality control on the battery production line. Using the model, it proved straightforward to discriminate between viable and non-viable batteries based on the temperature dependence of the electrochemical reaction kinetics at the electrodes, the average diffusion coefficients and the charge transfer resistances. Furthermore, as well as marked differences, for example, between the time constants, activation energies, polarisation resistances of the viable and non-viable batteries, the individual contributions of the anodes and cathodes in the batteries were de-convoluted and interpreted through the model framework.

1. Introduction

Secondary lithium ion batteries are ubiquitous in portable electronic devices and are finding increasing application in hybrid electric vehicles [1,2]. During the charging of such devices, Li ions de-insert from the cathode [3] (typically comprised of metal oxides of the form Li_xMO_2) and are inserted into graphite anodes [4] and vice versa on discharging. Due to the very high energy density of lithium ion batteries, quality control is of paramount importance in the production of these devices to ensure safety as well as durability. In order for these requirements to be met, it is essential that faults in batteries due to manufacturing errors, etc. can be detected rapidly and with high accuracy (i.e. with low incorrect rejection rates); preferably on the production line.

Batteries are generally characterized by using standard current/voltage (I/V) measurements [5] and by the more sophisticated Electrochemical Impedance Spectroscopy (EIS) [6]. The latter involves fitting EIS data to a theoretical model, based on

* Corresponding author.
E-mail addresses: pierrot.attidekou@newcastle.ac.uk, npsa5@ncl.ac.uk, aspierroti@gmail.com (P.S. Attidekou), simon.lambert@newcastle.ac.uk (S. Lambert), matthew.armstrong@newcastle.ac.uk (M. Armstrong), james.widmer@newcastle.ac.uk (J. Widmer), keith.scott@newcastle.ac.uk (K. Scott), paul.christensen@newcastle.ac.uk (P.A. Christensen).

http://dx.doi.org/10.1016/j.jpowsour.2014.06.064
0378-7753/

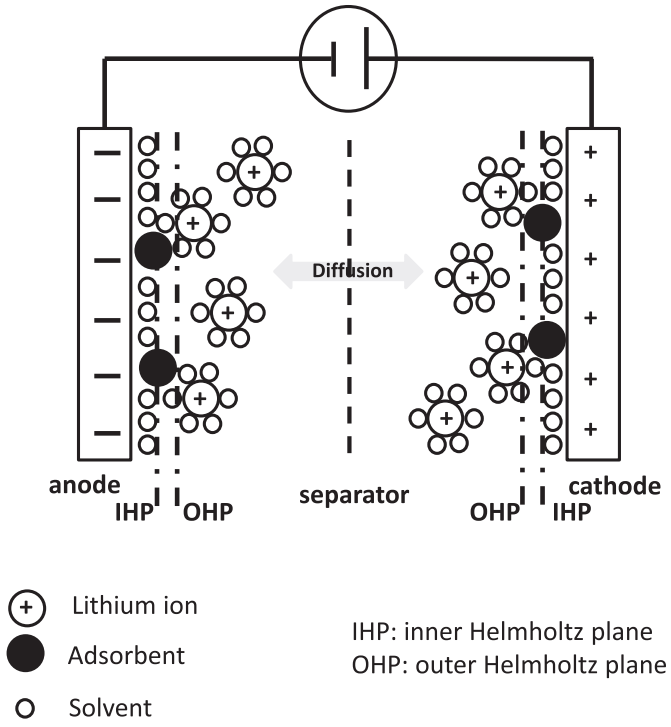

Fig. 1. Schematic representation of electrified interface.

circuitry comprising electronic components which may be correlated with specific elements (e.g. anode, cathode, electrolyte, etc.) and processes (e.g. diffusion) in the battery [7,8]. In this way, resistance due to the Solid Electrolyte Interface (SEI) layer, the charge transfer processes of the anode and cathode, the electrolyte and connector impedances, diffusion effects [9,10] and changes due to the electrochemical and chemical reactions [11] in the battery, etc. (see Fig. 1) can be deduced from a comparison of the theoretical model with experimental data. The rate constant of fast electron reactions can be also monitored [12].

EIS is also called AC impedance spectroscopy [13] and was first applied in the field of wet electrochemistry. It has been employed in corrosion studies where complicated processes involve surface and solution reactions. Moreover the technique has also been used extensively for lead acid battery characterisation. EIS often becomes a technique of choice to study the electrified interface and hence has been used in lithium ion batteries. Briefly, the EIS literature on lithium ion batteries may be represented by typical papers such as those by Zhuang et al. [14] and Chagnes and Swiatowska [15]. Chang and Park [16] have described and discussed the development of new EIS methods to reduce measurement time.

Typical lithium ion battery modelling using EIS is focused on the electrolyte and the porous electrodes/electrolyte interfaces in order to determine the optimum parameters for better batteries design and to characterise ageing effect [17]. Valuable information for diagnosing faults whilst in operation may be obtained and accurate State of Charge (SOC) determined [18]. There are many models utilising equivalent circuits to describe the electrochemical behaviour of lithium ion batteries, the simplest is the single particles (SP) model [19]. Other models include, in order of increasing sophistication (i.e. decreasing maximum error rate: the Internal Resistance (IR) model, One Time Constant (OTC), Two Time Constants (TTC)) to try to better monitor the cell dynamics [20,21], the Rint, the RC, the Thevenin [22], the partnership for a new generation of vehicle (PNGV) [23] and the improved Thevenin or Dual Polarisation (DP) model [24]. Of all the models above, DP model characterises most accurately the dynamics of the lithium ion battery and provides the most accurate estimation of SOC. It was found that we could only fit the data from the Saft batteries with multiple time constants and hence we employed a variation of the DP model.

Another consideration in the field of failure diagnosis is to monitor the temperature. Temperature imbalance has been observed in batteries, and this can lead to unexpected performance and life degradation [25]. Such problems are related to battery design. Thus, in a cylindrical battery [26], the centre is slightly warmer than the exterior which leads to preferential reactions at the centre upon charge and discharge. In a prismatic cell [27] the temperature gradient is different due to the difference in shape and in particular the fact that the latter are generally very thin and dissipate heat more effectively.

In general, physical processes taking place in galvanic cells may be distinguished on the basis of their time constants, and hence frequency dependent responses. Thus, high frequency behaviour is dominated by the inductive response of the connecting leads, the medium frequency range by the charge transfer at the electrodes/electrolyte interfaces and the low frequency region by diffusion of lithium ions through the electrode matrix and SEI layer [28].

This paper presents initial studies aimed at developing a non-invasive, EIS-based system for the rapid characterization of vehicular lithium ion batteries. The work reported in this paper was

Table 1
List of symbols.

Symbol/unit	
L/H	Inductance
R/Ω	Resistance
R_p/Ω	Polarisation resistance
R_{ct}/Ω	Charge transfer resistance
R_w/Ω	Warburg resistance
CPE (Q)	Constant phase element (capacitance)
τ/s	Time constant
τ_w/s	Warburg time constant
T/K or Celsius	Temperature
Y_0/S $s^{1/2}$	Admittance
w/rad s^{-1}	Angular frequency
K	Rate constant
A	Pre-exponential factor
E_a/J mol^{-1}	Activation energy
R/J mol^{-1} K^{-1}	Universal gas constant
σ/Ω s^{-1}	Diffusion coefficient
Z_w	Warburg impedance
SOC	State of Charge

Table 2
Electrical characteristics of the supplied batteries.

Nominal voltage	3.6 V
Typical capacity (C rate, +20 °C)	41 Ah
Minimum capacity (C rate, +20 °C)	40 Ah
Maximum voltage (continuous)	4.0 V
Maximum voltage (pulse)	4.1 V
Minimum voltage (continuous)	2.7 V
Minimum voltage (pulse)	2.0 V

Table 3
Mechanical characteristics of the VL41M batteries.

	VL41M sleeved	VL41M formed
Diameter	55.0 mm max.	54.6 mm max.
Height	223 mm max.	222.8 mm max.
Weight	1.1 kg max.	1.1 kg max.

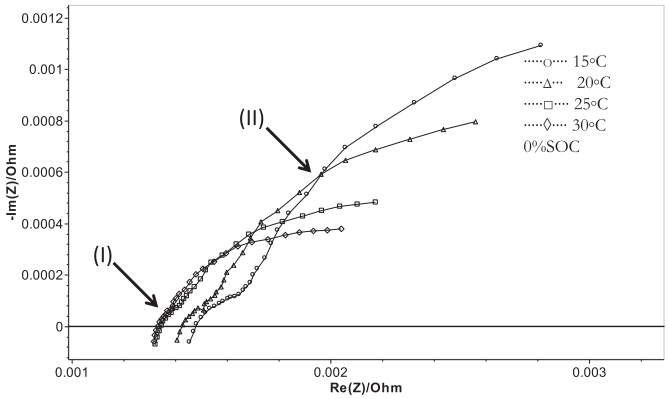

Fig. 2. Nyquist plots of battery 1 from EIS at 0% SOC at 15 °C (···○···), 20 °C (···Δ···), 25 °C (···□···) and 30 °C (···◇···).

carried out at zero state-of-charge (0% SOC) i.e. 3.2 V, where SOC is defined as the ratio of the energy available to the total energy capacity of the battery [29] expressed as a percentage, as a function of temperature. A subsequent paper will report studies as a function of SOC at constant temperature. Two batteries (see Table 1) were supplied by Saft (Bordeaux France), one chosen as representative of a viable battery (battery 2), the other (battery 1) chosen on the basis of having a significantly faster self-discharge rate than the other (i.e. 3.940 mV day^{-1} in comparison to 2.108 mV day^{-1}). Given that both cells exhibited self-discharge, 0% SOC was chosen as the capacity at which measurements would be taken in order to provide a fixed point of reference.

Current practice is for batteries to be rejected on the basis of enhanced self-discharge rates. This requires, typically, two weeks of monitoring compared to less than 10 min with the present technique. With further optimisation and refining we believe a test time of ca. 1 min is achievable.

2. Experimental methods

A set of impedance spectra were recorded on the two cylindrical, Saft Li-ion VL41M batteries at 0% SOC and at various temperatures. The electrical specifications of the batteries are summarised in Table 2 and the mechanical properties in Table 3. Battery testing was performed using a Bio-logic HP1005/VMP3B-100 electrochemical impedance analyser.

The batteries were placed in an environmental simulation chamber (Binder GmbH) capable of maintaining a constant

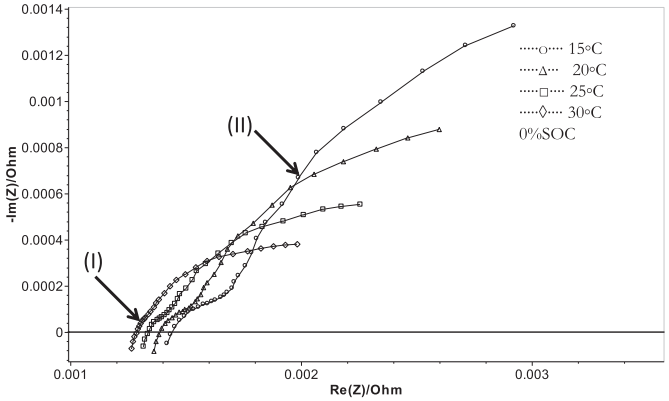

Fig. 3. Nyquist plots of battery 2 from EIS at 0% SOC at 15 °C (···○···), 20 °C (···Δ···), 25 °C (···□···) and 30 °C (···◇···).

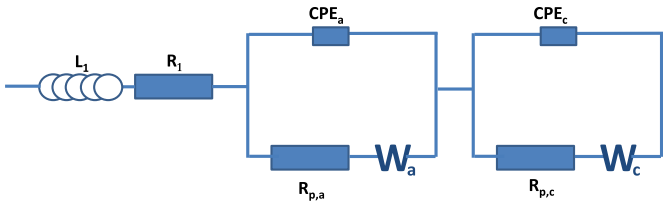

Fig. 4. A schematic of the equivalent circuit for non-linear least square fitting.

temperature over the range −40 to 180 °C. The batteries were allowed to reach thermal equilibrium over 12 h before testing. The primary aim of the work reported in this paper was to determine if, and to what extent, the EIS responses of the two batteries could be discriminated. Thermocouples were connected to the top and the bottom of each battery to monitor temperature variation within the batteries. EIS sweeps were performed at stable battery temperatures of 15, 20, 25 and 30 °C.

The batteries were discharged using constant current (CC) at a rate of $C/10$ to the desired voltage 3.2 V followed by constant voltage (CV) until the current fell to zero, to ensure equilibrium at 0% SOC. The batteries were held at this voltage for 3 h before each EIS experiment was performed.

The EIS experimental conditions were: perturbation voltage amplitude, $V_a = 3$ mV over the frequency range 1 kHz to 100 mHz, at ten points per decade.

Table 4
Fitting parameter values for impedance spectra measured at 15, 20, 25 and 30 °C.

	$T = 15$ °C	$T = 20$ °C	$T = 25$ °C	$T = 30$ °C
(a) Parameters for battery 1				
L_1/H ($\times 10^{-6}$)	0.2382 (±0.0061)	0.1570 (±0.0077)	0.3130 (±0.0059)	0.2266 (±0.0087)
R_1/Ω ($\times 10^{-3}$)	1.407 (±0.007)	1.397 (±0.007)	1.128 (±0.004)	1.291 (±0.005)
CPE_a/F s^{-n} ($\times 10^{-3}$)	20.91 (±0.23)	8.78 (±0.10)	77.34 (±0.11)	96.52 (±0.01)
CPE_c/F s^{-n} ($\times 10^{-3}$)	1.70 (±0.27)	1.721 (±0.17)	64.27 (±0.01)	7.46 (±0.04)
$R_{p,a}/\Omega$ ($\times 10^{-6}$)	1815 (±7.868)	1541 (±7.007)	56.73 (±3.565)	0.386 (±0.087)
$R_{p,c}/\Omega$ ($\times 10^{-6}$)	240 (±2.542)	132 (±1.813)	140 (±1.635)	4.031 (±0.291)
ΣZ_w ($\times 10^{-3}$)	5.19 (±0.05)	5.70 (±0.04)	6.61 (±0.03)	7.35 (±0.04)
$n_2 = n_3$	0.86	0.86	0.86	0.86
χ^2 ($\times 10^{-3}$)	3.145	0.903	0.859	0.523
Residual standard error ($\times 10^{-6}$)	4.916	4.807	3.27	3.132
(b) Parameters for battery 2				
L_1/H ($\times 10^{-6}$)	0.2429 (±0.0058)	0.2280 (±0.0061)	0.2872 (±0.0171)	0.2378 (±0.0054)
R_1/Ω ($\times 10^{-3}$)	1.375 (±0.005)	1.325 (±0.005)	1.245 (±0.008)	1.229 (±0.003)
CPE_a/F s^{-n} ($\times 10^{-2}$)	2.00 (±0.43)	1.85 (±0.18)	1.85 (±0.04)	1.98 (±0.05)
CPE_c/F s^{-n} ($\times 10^{-2}$)	1.43 (±0.01)	1.63 (±0.01)	1.61 (±0.01)	8.53 (±0.01)
$R_{p,a}/\Omega$ ($\times 10^{-6}$)	2543 (±7.868)	1588 (±4.064)	1012 (±5.657)	2.653 (±2.403)
$R_{p,c}/\Omega$ ($\times 10^{-6}$)	258 (±7.868)	199 (±7.401)	172 (±4.664)	22.46 (±0.507)
ΣZ_w ($\times 10^{-3}$)	4.80 (±0.05)	5.38 (±0.08)	6.19 (±0.03)	6.99 (±0.04)
$n_2 = n_3$	0.86	0.86	0.86	0.86
χ^2 ($\times 10^{-3}$)	1.027	1.729	0.647	0.404
Residual standard error ($\times 10^{-6}$)	5.901	4.403	3.176	3.1

The figures in brackets are the relative standard errors in each parameter.

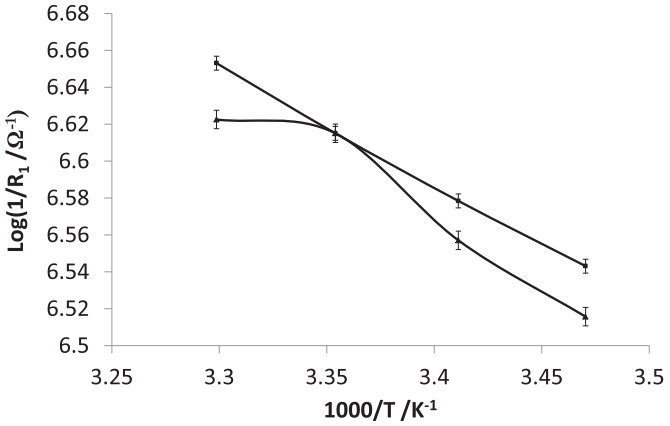

Fig. 5. Arrhenius plot battery 1 (···▲···) and battery 2 (···■···) at 0% SOC.

The fitting of the data so obtained was conducted using EC-Lab software (Zfit). The computer program employed for analysis by Zfit was based on a complex, Non-Linear Least Squares (NLLS) fitting of the model parameters of the impedance spectrum to the measured spectrum. NLLS starts with initial model parameters provided by the user. These parameters are then employed in the algorithm which changes these values by an iterative method and evaluates the resulting fit. If the fit is improved, the new parameter is accepted; in contrast, if the fit is not improved the previous parameter is retained and a different one is changed and the test repeated until the iteration converges to a criterion of acceptance evaluated by chi-square (χ^2) which is defined according to:

$$\chi^2 = \sum_{i=1}^{n} \frac{|Z_{\text{meas}}(i) - Z_{\text{model}}(f_i, \text{param})|^2}{\sigma_i^2} \quad (1)$$

where $Z_{\text{meas}}(i)$ is the measured impedance at the frequency f_i, Z_{model} (f_i, param) is the calculated impedance based on the chosen model, f_i is the frequency and σ_i is the standard deviation that can be equated to the weight of the impedance data points and this can be used to select the good circuit with low level of noise. In addition, the relative error of the total impedance versus frequency indicates a good fit and is highly relevant in evaluating the acceptability of the equivalent circuit. The relative error (normalised to Z) is defined as follows:

$$\Delta|Z|(\%) = (|Z|_{\text{meas}} - |Z|_{\text{calc}})/|Z|_{\text{meas}} \times 100 \quad (2)$$

where $Z_{\text{meas}}(i)$ is the measured impedance at the frequency f_i and Z_{calc} the calculated impedance deriving from the model employed. The overall result represents an optimisation of the fit over the entire spectrum. Various factors such as choosing an incorrect model, poor estimation of the initial values or noise can prevent convergence of the fit.

The data were also analysed for Non-Linear Least Squares (NLLS) fit using the R program. This was employed in order to extract the residual standard error as well as to evaluate the fit.

3. Results and discussion

The Nyquist plots of batteries 1 and 2 at 0% SOC and 15, 20, 25 and 30 °C are shown in Figs. 2 and 3 respectively. The impedance plots in these figures may be represented as the superposition of two impedance arcs. A small impedance arc (I) can be seen in the medium frequency range and a relatively large one in the medium to low frequency range (II). A decrease in the width and height of both impedance arcs can be observed with increasing temperature, as well as a shift of the intercepts of the plots on the real axis to lower resistance values. The intercept value decreases from 1.407×10^{-3} Ω at 15 °C to 1.291×10^{-3} Ω at 30 °C for the non-viable battery 1, and from 1.375×10^{-3} Ω at 15 °C to 1.229×10^{-3} Ω at 30 °C for the viable battery 2.

An equivalent circuit (EC) was designed for this study and is shown in Fig. 4. A number of equivalent circuits have been proposed in the literature. Different combination of elements gives rise to different equivalent circuitries for EIS models depending on the considered chemistry [30].

The fact that the Nyquist plots in Figs. 2 and 3 show depressed semi-circles in the high to medium frequency domain suggested that the inclusion of CPEs in the modified Randles circuit would be appropriate, and this differentiates our model from the DP approach; our model may be considered as one consisting of multiple time constants [31] as opposed to only two. A process of iteration using these elements at the anode and cathode resulted in the proposed model assuming a finite length diffusion component (W_a and W_c) at both electrodes.

The proposed EC can be described as a combination of an inductance component (L_1) connected in series with an Ohmic resistance (R_1) which in turn is connected in series with two modified Randles circuits comprising a parallel combination of constant phase elements CPE_a and CPE_c that represent the double layer capacitance in series with polarisation resistances ($R_{p,a}$ and $R_{p,c}$), also known as charge transfer resistances, and Warburg impedances (W_a and W_c). The overall EC can be formulated as: $[L_1 + R_1 + ((CPE_a)/(R_{p,a} + W_a)) + ((CPE_c)/(R_{p,c} + W_c))]$ where subscript 'a' refers to anode and 'c' to cathode. Constant phase elements (CPEs) are used to model the behaviour of imperfect dielectrics, and the electrical impedance of the CPEs (Z_{CPE}) may be described by [32]:

$$Z_{\text{CPE}} = 1/(jw)^n\tau \quad (3)$$

where ω is the angular frequency of the AC signal (rad s^{-1}), and τ is the time constant in F cm^{-2} s^{n-1}, with $0 \leq n \leq 1$. When $n = 1$, it corresponds to a pure capacitor, and when $n = 0$ to a pure resistor. The Warburg components in both electrodes represent lithium ion diffusion processes into the electrode matrix and gives rise to a complex impedance, Z_w, generally defined according to:

$$Z_w = R_w \tanh([jw\tau_w]^n)/((jw\tau_0)^n) \quad (4)$$

where R_w is the Warburg resistance (Ω), τ_w [33] a constant in (seconds) and n varies between 0 and 1.

Non-linear Least Squares (NLLS) fits were made of the data in Figs. 2 and 3, based on the EC represented in Fig. 3 and the fitting parameters are given in Table 4(**a**) for battery 1 and Table 4(**b**) for battery 2. The chi-square (χ^2) values obtained were all ca. $\leq 10^{-3}$. Typical plots of the error between the model and experimental data from the EC-Lab software (Zfit) are shown in Figs. 6(a–d) and 7(a–d). As can be seen, the error is between 0.6 and 2.4%. Moreover, the residual standard error was found to be ca. 10^{-6} using the R program, see Table 4(**a**) and (**b**).

In this study, the high frequency range with negative values of −Im(Z) are ignored. This range is reported [34] to be associated with an inductive component (L_1) attributable to the connecting leads.

The intercept of the impedance spectrum with the real impedance Re(Z) axis (i.e. [−Im(Z) = 0]) represents the total Ohmic resistance [35,36] of the battery (R_1) which is associated with the combined resistance of the electrolyte, current collectors, separators, the electronic resistance of the active particles of the anode

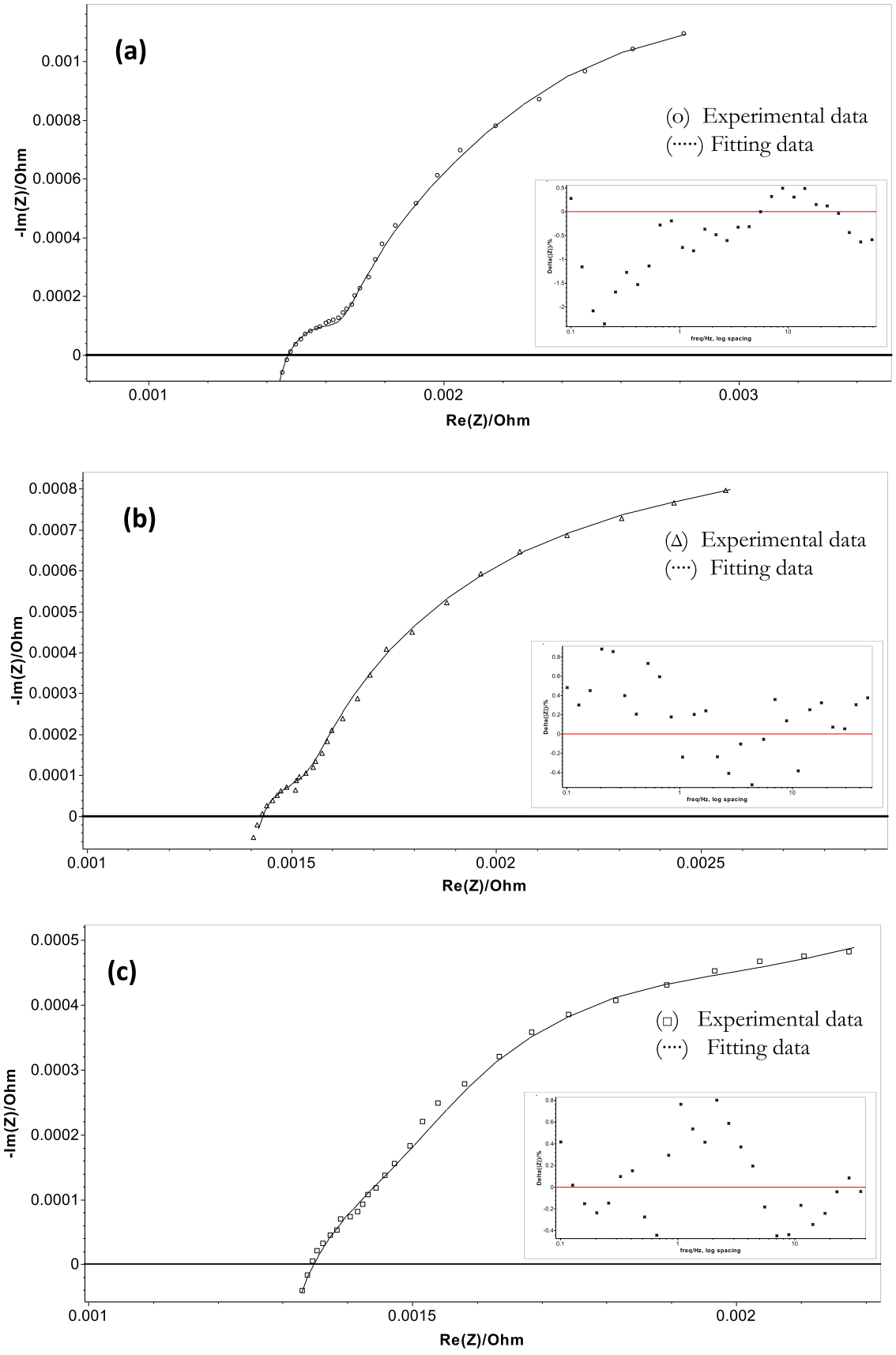

Fig. 6. Nyquist plots of battery 1 at 0% SOC, at various temperature and model simulation (·····) and χ^2 values: (a) 15 °C (○) with $\chi^2 = 3.145 \times 10^{-3}$; (b) 20 °C (△) with $\chi^2 = 0.9034 \times 10^{-3}$; (c) 25 °C (□) with $\chi^2 = 0.8595 \times 10^{-3}$; (d) 30 °C (◇) with $\chi^2 = 0.5227 \times 10^{-3}$. The insert shows the relative residuals (normalized to $|Z|$ as a function of frequency).

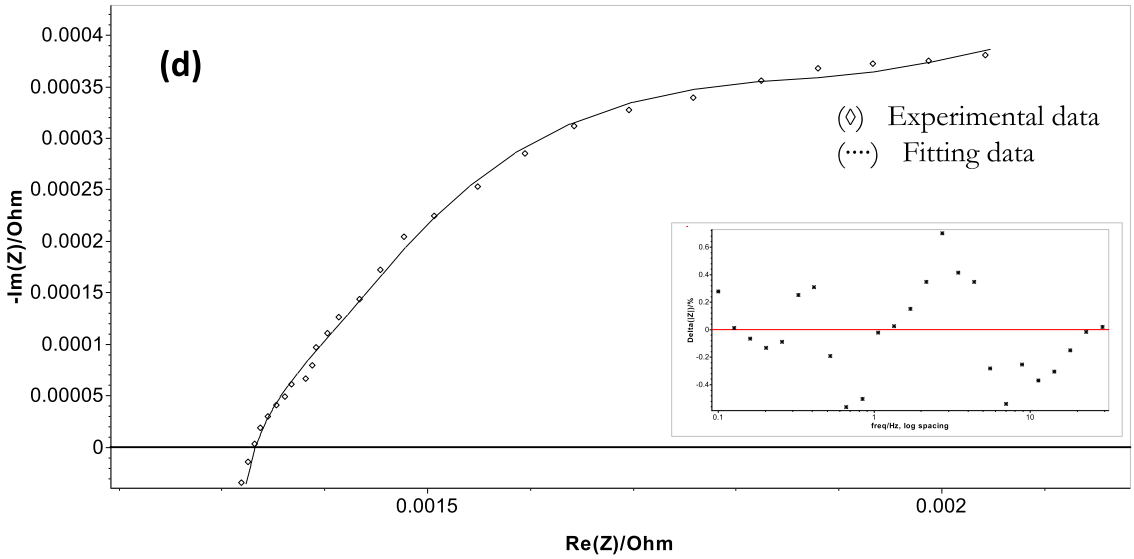

Fig. 6. (*continued*).

and cathode materials and the electrical contacts [37]. From Figs. 2 and 3, this Ohmic resistance decreases with increasing temperature, which is most likely due to the ionic resistance of the electrolyte; which is temperature dependent. However, this may include the bulk resistance of the electrodes.

The variation of $\log(1/R_1)$ as function of inverse temperature for batteries 1 and 2, from the data in Figs. 1 and 2, is plotted in Fig. 5. As may be seen from the figure, for battery 2, there is a linear variation in agreement with Arrhenius behaviour [38], according to:

$$k = Ae^{-E_a/(RT)} \tag{5}$$

where E_a is the activation energy (J mol^{-1}), R the gas constant ((J mol^{-1} K^{-1}) and T the temperature (K). The slope of the plot inFig. 5 gives an activation energy for battery 2 of ca. 5.3 kJ mol^{-1}.

This result is in reasonable agreement with the literature, where such relatively low values of activation energy are associated with fresh batteries having undergone few charge/discharge cycles. The latter generally result in an increase in activation energy due to an increase in the thickness of the SEI layer on the anode. Thus Zhang et al. [39] have reported an activation energy of 4.3 kJ mol^{-1} for a fresh battery utilising a $LiFePO_4$ cathode; this increased to 20.9 kJ mol^{-1} after 300 cycles. However, an activation energy of 3.6 kJ mol^{-1} for a battery employing a $LiNiO_2$ cathode has also been reported [40], which decreased to 2.4 kJ mol^{-1} after 5250 cycles. Overall it appears that the activation energy observed is dependent upon battery history.

As stated above, battery 1 exhibited increased self-discharge; this coupled with the non-linear behaviour in Fig. 5, suggests that the battery had a fault.

The capacitive arc observed in the medium frequency range in the Nyquisyt plots in Figs. 6(a–d) and 7(a–d), modelled with a modified Randles circuit, is generally attributed to the SEI layer on the anode [41] convoluted with diffusion processes (R_w). The second arc, observed in the medium frequency region, which is generally also modelled with a modified Randles circuit, may be attributed to the effect of the charge transfer resistance at the electrode interface [42], also convoluted with diffusion processes (R_w). The two capacitive arcs are separated due to the different time constants for the processes involved.

The spectra in Figs. 6(a–d) and 7(a–d) appear as the superposition of two impedance arcs in the medium to low frequency range as discussed above. Both impedance arcs seem to follow the same trend in that their widths decrease as temperature increases. For battery 1, both impedance arcs merge together as the temperature is increased and essentially cannot be distinguished from one another at 25 and 30 °C, in contrast to the spectra collected at 15 and 20 °C. The same trend is observed for battery 2; however the arcs are only indistinguishable at 30 °C. The separation of the impedance arcs, and hence the electrochemical phenomena associated with them, is related to the time constant of the battery [43].

In lithium batteries, the electrochemical processes at the anode and cathode are different and hence may be expected to exhibit different time constants which are obtained from the following equation:

$$\tau = (RQ_0)^{1/n} \tag{6}$$

where τ is the time constant in second, R is the resistance in Ω, Q_0 is the capacitance (F).

This is indeed observed for both batteries 1 and 2 as shown in Fig. 8(a) and (b), where the logarithm of the time constant for the anode and cathode of batteries 1 and 2 are plotted as a function of temperature (at 0% SOC).

At temperatures <25 °C, the time constants associated with the processes taking place in battery 1 are estimated to be 5.55×10^{-3}, 7.62×10^{-3}, 6.46×10^{-4} and 8.09×10^{-6} s at the cathode at 15, 20, 25 and 30 °C respectively. At the anode, the time constants are 1.076×10^{-4}, 0.879×10^{-4}, 2.81×10^{-4} and 1.04×10^{-5} s at 15, 20, 25 and 30 °C, respectively. The time constants for battery 1 are smaller at higher temperature (see Fig. 8(a)), as may be expected for activation controlled processes. However, it is clear that the time constants at the cathodes are greater than at the anodes at temperatures <25 °C in both batteries, but the rates become comparable at temperatures ≥25 °C.

For battery 2 the time constants at the cathode were 6.35×10^{-3}, 5.14×10^{-3}, 4.34×10^{-3} and 3.76×10^{-4} s at 15, 20, 25 and 30 °C, respectively whereas at the anode the values obtained were 1.95×10^{-5}, 0.967×10^{-5}, 0.584×10^{-5} and 8.36×10^{-5} s at 15, 20, 25 and 30 °C, respectively.

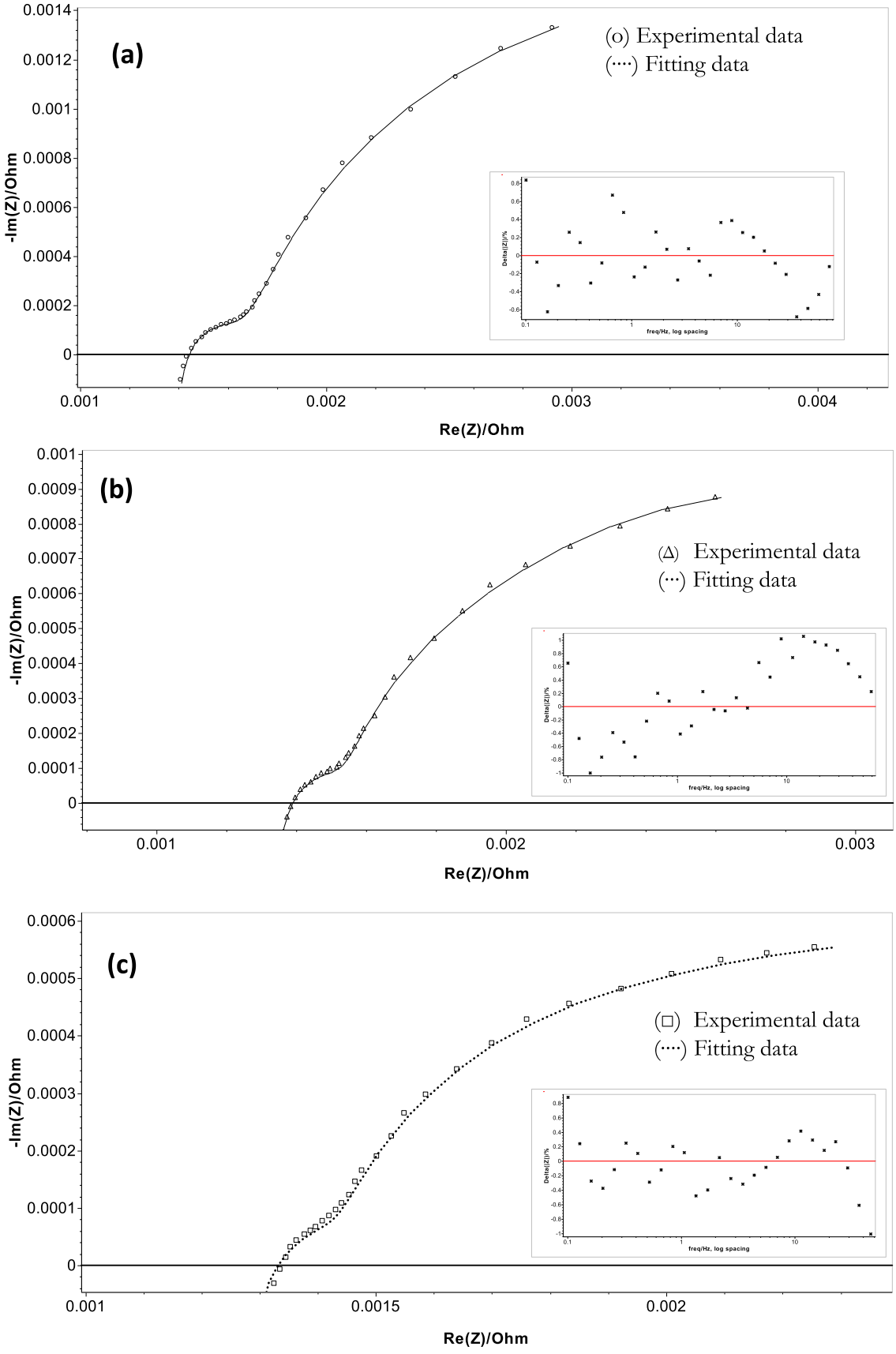

Fig. 7. Nyquist plots of battery 2 at 0% SOC, with change in temperature and model simulation (·····) and χ^2 values :(a) 15 °C (○) with $\chi^2 = 1.027 \times 10^{-3}$; (b) 20 °C (△) with $\chi^2 = 1.729 \times 10^{-3}$; (c) 25 °C (□) with $\chi^2 = 0.6467 \times 10^{-3}$; (d) 30 °C (◇) with $\chi^2 = 0.404 \times 10^{-3}$. The insert shows the relative residuals (normalized to $|Z|$ as a function of frequency).

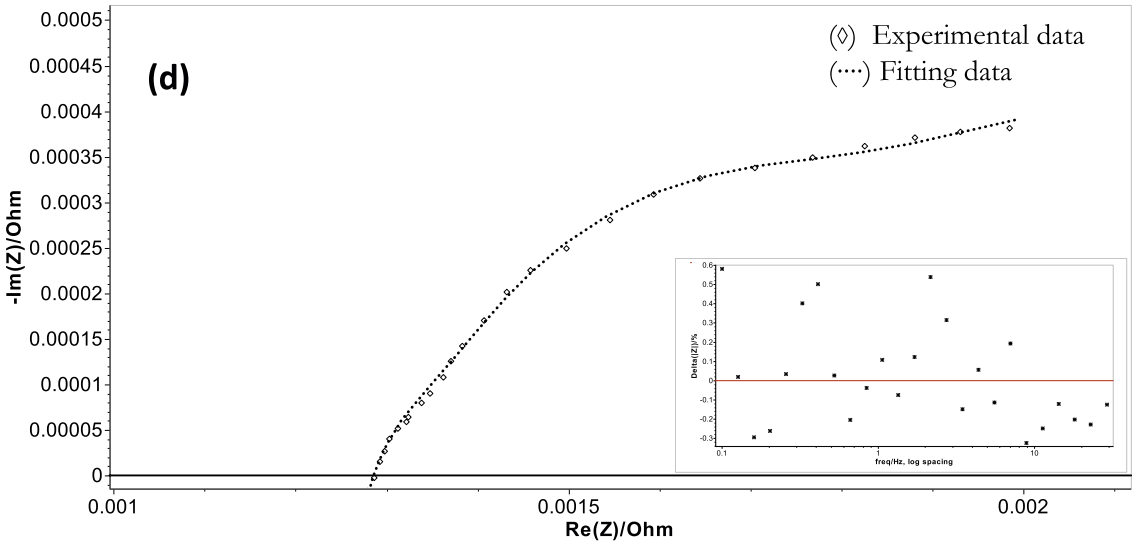

Fig. 7. (*continued*).

For battery 2 (Fig. 8(b)), the time constants at the cathode are also markedly faster than that at the anode at all temperatures <30 °C. Thus Fig. 8(a) and (b) again clearly shows that the electrochemical processes occurring in both electrodes can be discriminated for both batteries.

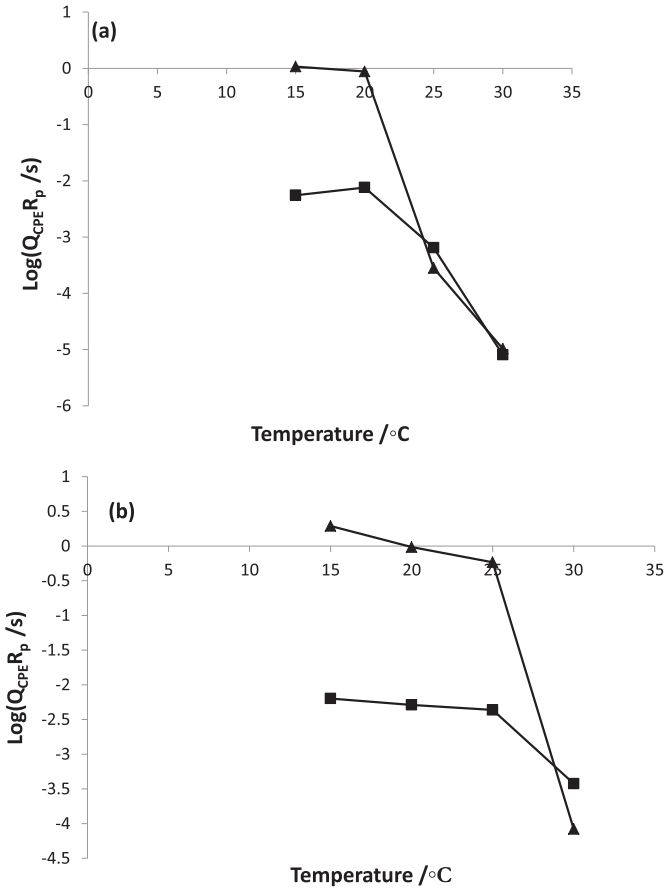

Fig. 8. (a) Variation of log(time constant) with temperature for battery 1 at 0% SOC (temperatures of 15, 20, 25 and 30 °C); (b) variation of log(time constant) with temperature for battery 2 at 0% SOC (temperatures of 15, 20, 25 and 30 °C).

The data in Fig. 8(a) and (b) also support the fact that there is a problem with battery 1. Whilst both batteries show a transition in behaviour in terms of the variation in time constant with temperature, this transition takes place at lower temperature in the non-viable battery 1.

Battery 2 also shows a transition in terms of the time constants, but only at 30 °C. The behaviour of both batteries is reflected in Fig. 9(a) and (b), which show the variation in $\log R_{p,a}$ and $\log R_{p,c}$ with temperature. The resistance of the anode is dominated by the SEI layer and the polarisation resistance; the cathode resistance is totally different from the anode [44]. Thus the decrease in the width of the impedance arcs with increase temperature in Figs. 1 and 2 is directly related to the decrease in $R_{p,c}$ and $R_{p,a}$. In battery operation when electrons enter an electrode, lithium ions diffuse through the electrode structure and out into the electrolyte (charge transfer). It seems reasonable to postulate that the total resistance of the anodes in each battery may include the resistances of the SEI layers [45] and the charge transfer resistances [46]. However, experimentally it was observed that increasing temperature results in a decrease of $R_{p,a}$ for both batteries (see Tables 1 and 2) and hence to a decrease in charge transfer resistance that leads to the transition observed in Fig. 9(a) and (b).

The variation of capacitance with temperature (shown as log[C] versus T) is depicted in Fig. 10(a) and (b) for batteries 1 and 2 respectively. For battery 2, Fig. 10(b), the capacitive response of the anode changes little with temperature, in contrast to the cathode which shows a constant capacitance at low temperature before decreasing at 30 °C. This behaviour can be related to the charge transfer taking place at the electrode/electrolyte interfaces, as capacitive processes are caused by discharge/charge of the electrode surface as a result of potential variations. The change in capacitance observed at 30 °C may suggest a structural change or SEI formation at the surface of the cathode. However the capacitive response of battery 1, see Fig. 10(a), does not resemble that observed for battery 2; exhibiting a somewhat random variation with temperature at both cathode and anode. It is clear from Fig. 10(a) and (b) that we are able to discriminate (again) between the viable and non-viable batteries. However, further work at different SOC, and an investigation of self-discharge are required to understand and interpret the data in Fig. 10(a) and (b).

It is not unreasonable to postulate that both the diffusion of lithium ions through the electrolyte and the intercalation of these

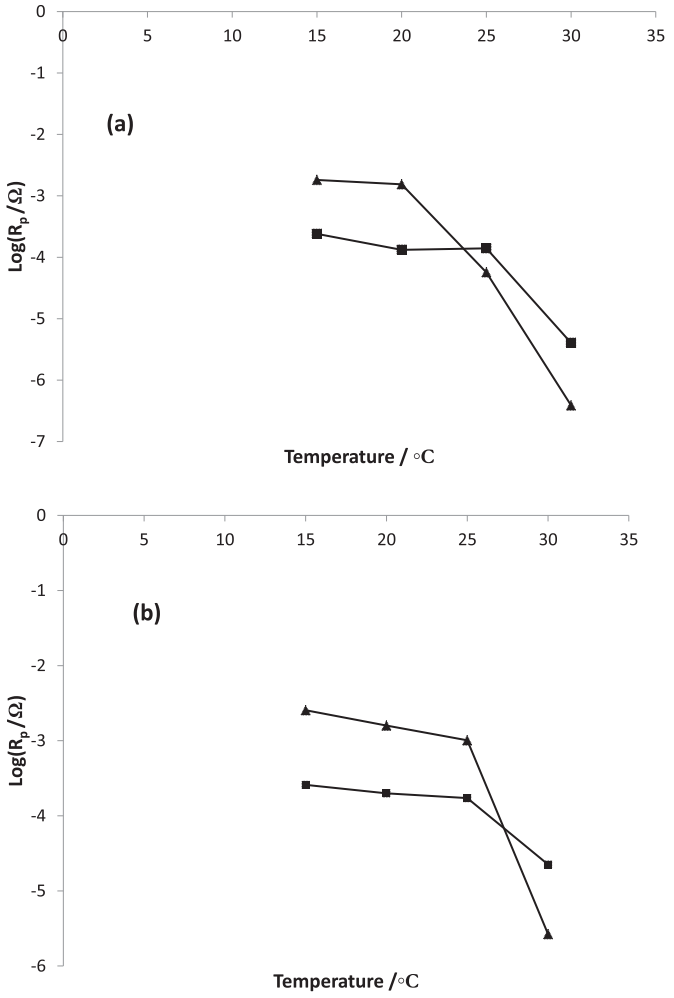

Fig. 9. Variation of the polarisation resistance versus temperature (a): log(R_p) at the anode (···▲···) and the cathode (···■···) for battery 1 at 15, 20, 25 and 30 °C and (b) log(R_p) at the anode (···▲···) and the cathode (···■···) for battery 2 at 15, 20, 25 and 30 °C.

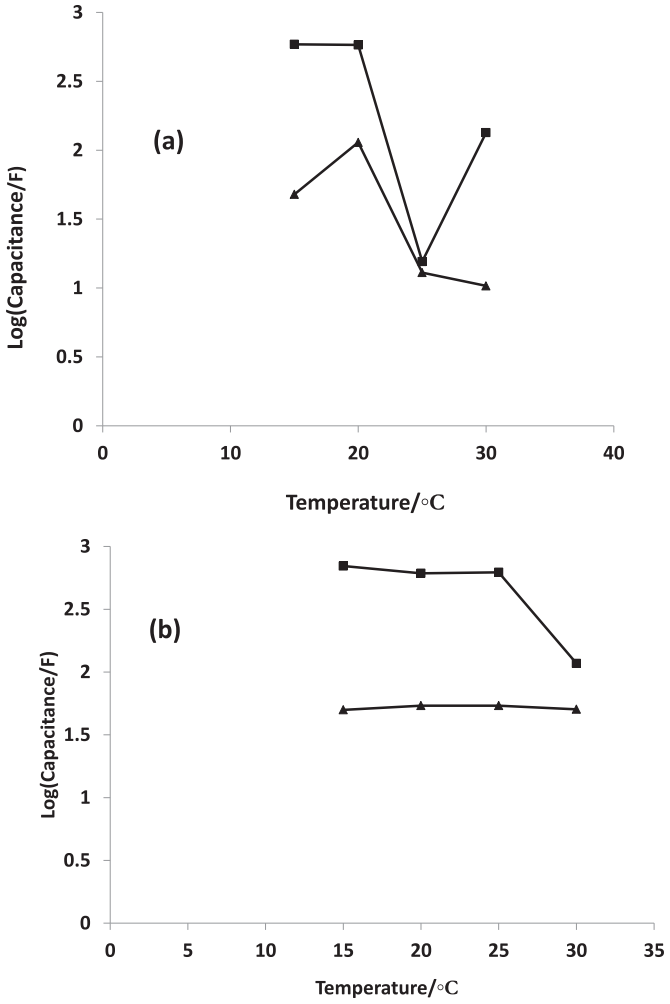

Fig. 10. Variation of the capacitance versus temperature (a) for battery 1 and (b) for battery 2.

ions are facilitated by increasing temperature. Hence, with respect to the former process, we would expect $R_{p,a}$ and $R_{p,c}$ to decrease with increasing temperature, and this in broad terms, was indeed observed in our data and by others [47].

Diffusion at the electrodes/electrolyte interfaces usually dominates the low frequency domain in impedance spectra, and this is, of course, temperature dependant [48]. The total impedance of an electrochemical battery at a particular frequency comprises the real and imaginary components of the anode and the cathode convoluted together. Persson et al. [49] have demonstrated extremely high mobility of lithium ions between the layers of graphite. We postulate a contribution of diffusion processes to the impedance of the anode as well as to the cathode and this is supported by the work of Xu et al. [50] on a Li/graphite half cell. They observed a spike in the low frequency domain that was attributed to long range ion diffusion in the bulk of the graphite. The angle with the real axis of the spike was seen to change with cell potential from 90° progressively to 45°, which is characteristic of semi-infinite diffusion. However, in order to determine the diffusional contribution of lithium ions into the anode and cathode structure, measured at low frequency, a three electrode battery would be required, i.e. incorporating a reference electrode and this is not an option available for a sealed Li ion battery. The only parameter accessible is the average diffusion coefficient, σ ($\Omega\ s^{-1}$), of the lithium ions within the batteries via the admittance Y_0 ($S\ s^{1/2}$), σ from which can be evaluated according to [51]:

$$\sigma = 1\Big/\left(Y_0\sqrt{2}\right) \tag{7}$$

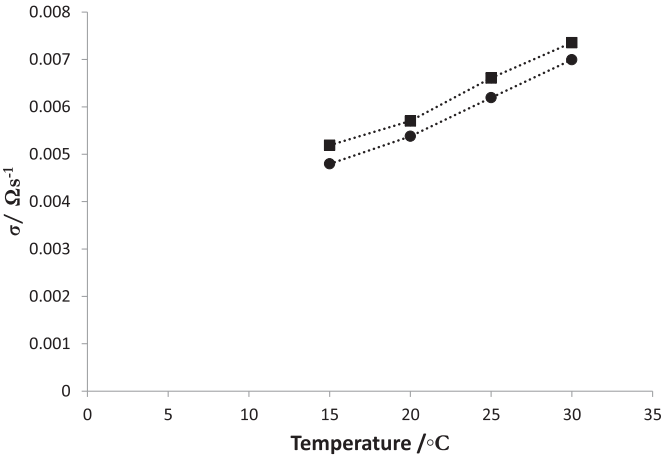

Fig. 11. Variation of diffusion coefficient versus temperature at 0% SOC, battery 1 (···■···); and battery 2 (···●···).

Fig. 10 shows plots of the σ versus temperature for batteries 1 and 2. From the data it is clear that, as expected, the diffusion coefficient of both batteries increases with temperature. In addition, the batteries again showed significantly different response and hence could be distinguished from each other (Fig. 11).

4. Conclusions

In order to develop a rapid, non-destructive, quality control method for lithium battery production, two commercial, 40 Ah high power lithium ion batteries (viable and non-viable) from Saft were investigated using electrochemical impedance spectroscopy as a function of temperature at 0% SOC. An equivalent circuit-based model was formulated to fit the experimental data in order to extract key battery parameters for analysis.

The impedance spectra of both batteries showed superimposed impedance arcs that exhibited marked dependence upon temperature; these arcs have been attributed to the SEI layer and to polarisation resistance. Because of the significant difference in time constant, the processes at the anode could be separated from those taking place at the cathode.

In depth analysis of the results has allowed discrimination between the viable and non-viable batteries on the basis of a number of parameters such as time constant, activation energy, polarisation resistances variation at electrodes with temperature, etc. In addition the model has allowed the interpretation of the data on the basis of physical processes taking place in the batteries.

This work has provided initial benchmark data on which a battery quality control system will be based.

Acknowledgements

This research was supported by the EU under Framework 7 grant agreement no: 285385 of European Li-Ion Battery Advanced Manufacturing for Electric Vehicles “ELIBAMA”. The authors also should like to acknowledge Saft for supplying the batteries employed in this work and for helpful guidance. The authors would like to thank Dr. A. Hamnett for useful discussions.

References

[1] B. Scrosati, J. Garche, J. Power Sources 195 (2010) 2419–2430.
[2] L.-X. Yuan, Z.-H. Wang, W.-X. Zhang, X.-L. Hu, J.-T. Chen, Y.-H. Huang, J.B. Goodenough, Energy Environ. Sci. 4 (2011) 269–284.
[3] J.-M. Tarascon, M. Armand, Nature 414 (15 November 2001).
[4] J.L. Jespersen, A.E. Tønnesen, K. Nørregaard, L. Overgaard, F. Elefsen, World Electr. Veh. J. ISSN: 2032-6653 3 (2009). AVERE.
[5] P.S. Attidekou, F. García-Alvarado, P.A. Connor, J.T.S. Irvine, J. Electrochem. Soc. 154 (3) (2007) A217–A220.
[6] H. Hu, S. Yurkovich, J. Power Sources 198 (2012) 338–350.
[7] C. Ho, D.I. Raistrick, R.A. Huggins, J. Electrochem. Soc. Electrochem. Sci. Technol. 127 (2) (1980) 343–350.
[8] C.T. Love, K. Swider-Lyons, Electrochem. Solid-State Lett. 15 (4) (2012) A53–A56.
[9] W. Lai, F. Ciucci, J. Electrochem. Soc. 158 (2) (2011) A115–A121.
[10] J. Song, M. Bazant, J. Electrochem. Soc. 160 (1) (2013) A15–A24.
[11] F. Ciucci, W. Lai, Electrochim. Acta 81 (2012) 205–216.
[12] J.E.B. Randles, Discuss. Faraday Soc. 1 (1947) 11–19.
[13] D.D. Macdonald, Electrochim. Acta 51 (2006) 1376–1388.
[14] Quan-Chao Zhuang, Xiang-Yun Qiu, Shou-Dong Xu, Ying-Huai Qiang, Shi-Gang Sun, in: Ilias Belharouak (Ed.), Lithium Ion Batteries – New Developments, InTech, 2012, ISBN 978-953-51-0077-5, http://dx.doi.org/10.5772/26749. Available from: http://www.intechopen.com/books/lithium-ion-batteries-new-developments/diagnosis-of-electrochemical-impedance-spectroscopy-in-lithium-ion-batteries.
[15] Alexandre Chagnes, Jolanta Swiatowska, in: Ilias Belharouak (Ed.), Lithium Ion Batteries – New Developments, InTech, 2012, ISBN 978-953-51-0077-5 http://dx.doi.org/10.5772/31112. Available from: http://www.intechopen.com/books/lithium-ion-batteries-new-developments/electrolyte-and-solid-electrolyte-interphase-layer-in-lithium-ion-batteries.
[16] B.-Y. Chang, S.-M. Park, Annu. Rev. Anal. Chem. 3 (2010) 207–229.
[17] U. Tröltzsch, O. Kanoun, H.-R. Tränkler, Electrochim. Acta 51 (2006) 1664–1672.
[18] J. Zhang, J. Lee, J. Power Sources 196 (2011) 6007–6014.
[19] A.P. Schmidt, M. Bitzer, Á.W. Imre, L. Guzzella, J. Power Sources 195 (2010) 5071–5080.
[20] S. Yoon, I. Hwang, C.W. Lee, H.S. Ko, K.H. Han, J. Electroanal. Chem. 655 (2011) 32–38.
[21] A. Rahmoun, H. BiechlElectr. Rev., Przegl. Elektrotech. ISSN: 0033-2097 88 (7b) (2012).
[22] Min Chen, Gabriel A. Rinćon-Mora, IEEE Trans. Energy Convers. 21 (2) (June 2006).
[23] P. Nelson, D. Dees, K. Amine, G. Henriksen, J. Power Sources 110 (2) (2002) 349–356.
[24] H. He, R. Xiong, J. Fan, Energies 4 (2011) 582–598, http://dx.doi.org/10.3390/en4040582.
[25] S. Al-Hallaj, J.R. Selman, J. Power Sources 110 (2) (2002) 341–348.
[26] Y. Inui, Y. Kobayashi, Y. Watase, Energy Convers. Manag. 48 (7) (2007) 2103–2109.
[27] P. Taheri, M. Bahrami, SAE Int. J. Passeng. Cars – Electron. Electr. Syst. 5 (1) (2012).
[28] Q.C. Zhuang, T. Wei, L.L. Du, Y.L. Cui, L. Fang, S.G. Sun, J. Phys. Chem. C 114 (2010) 8614–8621.
[29] Y. Hu, S. Yurkovich, J. Power Sources 198 (2012) 338–350.
[30] N. Cui, J.L. Luo, Electrochim. Acta 45 (2000) 3973–3981.
[31] J.P. Schmidt, P. Berg, M. Schönleber, A. Weber, E. Ivers-Tiffée, J. Power Sources 221 (2013) 70–77.
[32] T. Osaka, T. Momma, D. Mukoyama, H. Nara, J. Power Sources 205 (2012) 483–486.
[33] C.H. Chen, J. Liu, K. Amine, J. Power Sources 96 (2001) 321–328.
[34] A. Jossen, J. Power Sources 154 (2006) 530–538.
[35] P. Arora, B.N. Popov, R.E. White, J. Electrochem. Soc. 145 (1998) 807–815.
[36] S. Yoon, H. Kim, S.M. Oh, J. Power Sources 94 (2001) 68–73.
[37] J. Li, E. Murphy, J. Winnick, P.A. Kohl, J. Power Sources 102 (2001) 294–301.
[38] H. Schranzhofer, J. Bugajski, H.J. Santner, C. Korepp, K.-C. Möller, J.O. Besenhard, M. Winter, W. Sitte, J. Power Sources 153 (2006) 391–395.
[39] Y. Zhang, C.Y. Wang, X. Tang, J. Power Sources 196 (2011) 1513–1520.
[40] Y. Zhang, C.-Y. Wang, J. Electrochem. Soc. 156 (7) (2009) A527–A535.
[41] E. Karden, S. Buller, R.W. De Doncker, J. Power Sources 85 (2000) 72–78.
[42] S.-W. Kim, S.-I. Pyun, J. Electroanal. Chem. 528 (2002) 114–120.
[43] T. Momma, M. Matsunaga, D. Mukoyama, T. Osaka, J. Power Sources 216 (2012) 304–307.
[44] M.-S. Wu, P.-C.J. Chiang, J.-C. Lin, J. Electrochem. Soc. 152 (1) (2005) A47–A52.
[45] D.P. Abraham, M.M. Furczon, S.-H. Kang, D.W. Dees, A.N. Jansen, J. Power Sources 180 (2008) 612–620.
[46] C. Wang, A.J. Appleby, F.E. Little, Electrochim. Acta 46 (2001) 1793–1813.
[47] F. Huet, J. Power Sources 70 (1998) 59–69.
[48] D. Andre, M. Meiler, K. Steiner, Ch Wimmer, T. Soczka-Guth, D.U. Sauer, J. Power Sources 196 (2011) 5334–5341.
[49] K. Persson, V.A. Sethuraman, L.J. Hardwick, Y. Hinuma, Y.S. Meng, A. Van der Ven, V. Srinivasan, R. Kostecki, G. Ceder, J. Phys. Chem. Lett. 1 (8) (2010) 1176–1180.
[50] K. Xu, S. Zhang, R. Jow, J. Power Sources 143 (2005) 197–202.
[51] J. Gomez, R. Nelson, E.E. Kalu, M.H. Weatherspoon, J.P. Zheng, J. Power Sources 196 (2011) 4826–4831.